Biomedical Optics EXPRESS

Polarized multispectral imaging in a rigid endoscope based on elastic light scattering spectroscopy

Ji Qi,[1,2] Clement Barrière,[1,2] Tobias C. Wood,[1] and Daniel S. Elson[1,2,*]

[1]*Hamlyn Centre for Robotic Surgery, Institute of Global Health Innovation, Imperial College London, Exhibition Road, London SW7 2AZ, UK*
[2]*Department of Surgery and Cancer, Imperial College London, Exhibition Road, London SW7 2AZ, UK*
**ds.elson@imperial.ac.uk*

Abstract: Elastic light scattering spectroscopy (LSS) is widely utilized to investigate cellular structures in cultured cells and various tissues. However, few imaging systems, especially endoscopic imaging systems, can implement LSS. It is the aim of this work to create a polarized multispectral imaging system based around a rigid endoscope to detect micrometer sized particles using LSS. The instrument first validated with different sized mono-disperse polystyrene microspheres, then an image is reconstructed based on LSS which shows the differentiation of different sized microspheres. Finally a preliminary experiment is conducted to demonstrate its capability to discriminate different types of cells.

OCIS codes: (170.2150) Endoscopic imaging; (290.5855) Scattering, polarization; (110.4234) Multispectral and hyperspectral imaging.

References and links

1. D. G. Ferris, *Modern Colposcopy: Textbook and Atlas* (Kendall Hunt, 2004).
2. R. H. Riddell, H. Goldman, D. F. Ransohoff, H. D. Appelman, C. M. Fenoglio, R. C. Haggitt, C. hren, P. Correa, S. R. Hamilton, B. C. Morson, S. C. Sommers, and J. H. Yardley, "Dysplasia in inflammatory bowel disease: standardized classification with provisional clinical applications," Hum. Pathol. **14**(11), 931–968 (1983).
3. L. Perelman, V. Backman, M. Wallace, G. Zonios, R. Manoharan, A. Nusrat, S. Shields, M. Seiler, C. Lima, T. Hamano, I. Itzkan, J. Van Dam, J. Crawford, and M. Feld, "Observation of periodic fine structure in reflectance from biological tissue: a new technique for measuring nuclear size distribution," Phys. Rev. Lett. **80**(3), 627–630 (1998).
4. V. Backman, R. Gurjar, K. Badizadegan, I. Itzkan, R. R. Dasari, L. T. Perelman, and M. S. Feld, "Polarized light scattering spectroscopy for quantitative measurement of epithelial cellular structures in situ," IEEE J. Sel. Top. Quantum Electron. **5**(4), 1019–1026 (1999).
5. L. Qiu, D. K. Pleskow, R. Chuttani, E. Vitkin, J. Leyden, N. Ozden, S. Itani, L. Guo, A. Sacks, J. D. Goldsmith, M. D. Modell, E. B. Hanlon, I. Itzkan, and L. T. Perelman, "Multispectral scanning during endoscopy guides biopsy of dysplasia in Barrett's esophagus," Nat. Med. **16**(5), 603–606, 1p, 606 (2010).
6. L. T. Perelman, G. Zonios, V. Backman, R. Gurjar, I. Itzkan, R. R. Dasari, J. Van Dam, and M. S. Feld, "Quantitative analysis of mucosal tissues in patients using light scattering spectroscopy," Proc. SPIE **3597**, 474–479 (1999).
7. C. S. Mulvey, A. L. Curtis, S. K. Singh, and I. J. Bigio, "Elastic scattering spectroscopy as a diagnostic tool for apoptosis in cell cultures," IEEE J. Sel. Top. Quantum Electron. **13**(6), 1663–1670 (2007).
8. T. T. Wu and J. Y. Qu, "Assessment of the relative contribution of cellular components to the acetowhitening effect in cell cultures and suspensions using elastic light-scattering spectroscopy," Appl. Opt. **46**(21), 4834–4842 (2007).
9. C. S. Mulvey, K. Zhang, W. H. B. Liu, D. J. Waxman, and I. J. Bigio, "Wavelength-dependent backscattering measurements for quantitative monitoring of apoptosis, part 1: early and late spectral changes are indicative of the presence of apoptosis in cell cultures," J. Biomed. Opt. **16**(11), 117001 (2011).
10. C. S. Mulvey, K. Zhang, W. H. Bobby Liu, D. J. Waxman, and I. J. Bigio, "Wavelength-dependent backscattering measurements for quantitative monitoring of apoptosis, part 2: early spectral changes during apoptosis are linked to apoptotic volume decrease," J. Biomed. Opt. **16**(11), 117002 (2011).
11. J. R. Mourant, J. P. Freyer, A. H. Hielscher, A. A. Eick, D. Shen, and T. M. Johnson, "Mechanisms of light scattering from biological cells relevant to noninvasive optical-tissue diagnostics," Appl. Opt. **37**(16), 3586–3593 (1998).

#170838 - $15.00 USD Received 18 Jun 2012; revised 7 Aug 2012; accepted 8 Aug 2012; published 13 Aug 2012

12. O. C. Marina, C. K. Sanders, and J. R. Mourant, "Correlating light scattering with internal cellular structures," Biomed. Opt. Express **3**(2), 296–312 (2012).
13. H. Fang, M. Ollero, E. Vitkin, L. M. Kimerer, P. Cipolloni, M. M. Zaman, S. D. Freedman, I. J. Bigio, I. Itzkan, E. B. Hanlon, and L. T. Perelman, "Noninvasive sizing of subcellular organelles with light scattering spectroscopy," IEEE J. Sel. Top. Quantum Electron. **9**(2), 267–276 (2003).
14. I. J. Bigio, S. G. Bown, G. Briggs, C. Kelley, S. Lakhani, D. Pickard, P. M. Ripley, I. G. Rose, and C. Saunders, "Diagnosis of breast cancer using elastic-scattering spectroscopy: preliminary clinical results," J. Biomed. Opt. **5**(2), 221–228 (2000).
15. K. S. Johnson, D. W. Chicken, D. C. O. Pickard, A. C. Lee, G. Briggs, M. Falzon, I. J. Bigio, M. R. Keshtgar, and S. G. Bown, "Elastic scattering spectroscopy for intraoperative determination of sentinel lymph node status in the breast," J. Biomed. Opt. **9**(6), 1122–1128 (2004).
16. J. R. Mourant, T. M. Powers, T. J. Bocklage, H. M. Greene, M. H. Dorin, A. G. Waxman, M. M. Zsemlye, and H. O. Smith, "In vivo light scattering for the detection of cancerous and precancerous lesions of the cervix," Appl. Opt. **48**(10), D26–D35 (2009).
17. H. Suh, O. A'amar, E. Rodriguez-Diaz, S. Lee, I. Bigio, and J. E. Rosen, "Elastic light-scattering spectroscopy for discrimination of benign from malignant disease in thyroid nodules," Ann. Surg. Oncol. **18**(5), 1300–1305 (2011).
18. L. Qiu, V. Turzhitsky, E. Vitkin, L. Guo, E. Hanlon, I. Itzkan, and L. T. Perelman, "Coherent confocal light absorption and scattering spectroscopic microscopy," in *Biomedical Optics*, OSA Technical Digest (Optical Society of America, 2012), paper BSu4B.3.
19. K. Sokolov, R. Drezek, K. Gossage, and R. Richards-Kortum, "Reflectance spectroscopy with polarized light: is it sensitive to cellular and nuclear morphology," Opt. Express **5**(13), 302–317 (1999).
20. V. Backman, R. Gurjar, L. T. Perelman, V. Gopal, M. Kalashnikov, K. Badizadegan, A. Wax, I. Georgakoudi, M. Mueller, and C. W. Boone, "Imaging and measurement of cell structure and organization with submicron accuracy using light scattering spectroscopy," Proc. SPIE **4617**, 101–110 (2002).
21. R. S. Gurjar, V. Backman, L. T. Perelman, I. Georgakoudi, K. Badizadegan, I. Itzkan, R. R. Dasari, and M. S. Feld, "Imaging human epithelial properties with polarized light-scattering spectroscopy," Nat. Med. **7**(11), 1245–1248 (2001).
22. T. C. Wood and D. S. Elson, "Polarization response measurement and simulation of rigid endoscopes," Biomed. Opt. Express **1**(2), 463–470 (2010).
23. T. C. Wood and D. S. Elson, "Polarization characterisation of laparoscope systems for polarization resolved tissue imaging," in *Biomedical Optics*, OSA Technical Digest (CD) (Optical Society of America, 2010), paper BTuD29.
24. X. Wang and S. Yazdanfar, "Endoscope objective lens with large entrance pupil diameter and high numerical aperture," U.S. patent 7,821,720 (Oct. 26, 2010).
25. J. Qi, D. S. Elson, and C. Barriere, "Polarized multispectral imaging in a rigid endoscope based on polarized light scattering spectroscopy," in *Biomedical Optics*, OSA Technical Digest (Optical Society of America, 2012), paper BW4B.7.
26. C. F. Boliren and D. R. Huffman, *Absorption and Scattering of Light by Small Particles* (Wiley, New York, 1983).

1. Introduction

Epithelial dysplasia is an early form of pre-cancerous lesion recognizable in a traditional biopsy by a pathologist. The risk of high-grade dysplasia (carcinoma in situ) transforming into an invasive cancer is high but early diagnosis of dysplasia and carcinoma in situ allow surgical or other treatments to avoid this risk. The current clinical method for diagnosis of dysplasia in the gastrointestinal tract is investigational endoscopy which involves visual inspection and biopsy of high-risk tissue regions, followed by histopathological study [1]. Nevertheless it is still a great challenge to find the high risk sites because dysplasia is not necessarily observable under white light inspection, which leads to unnecessary and untargeted random biopsies. Moreover, it is an invasive, expensive and time consuming method which involves inconvenience to patients and is labor-intensive for clinicians [2].

In contrast, elastic light scattering spectroscopy (LSS) as a minimally invasive, fast, potentially automated and economical method can supplement and potentially replace the endoscopy-biopsy method. Cells in dysplasia are characterized by an enlarged nucleus with an irregular size and shape leading to different wavelength dependent scattering characteristics. LSS is able to resolve these scattering spectral characteristics. In particular, cell nuclei rather than the other smaller organelles in the cellular environment have a significant influence on the near-backward scattering spectrum [3–6]. Therefore morphological information on the cell nucleus can be obtained from backscattered spectra instead of traditional microscopic or flow

#170838 - $15.00 USD Received 18 Jun 2012; revised 7 Aug 2012; accepted 8 Aug 2012; published 13 Aug 2012

cytometric detection, neither of which is accessible *in situ*/*in vivo* in standard practice. LSS has previously been utilized to investigate cellular structures in cultured cells [7–13] and various tissues [5,14–17].

Many LSS systems utilize the polarization properties to differentiate multiple scattering and single scattering signals in turbid media such as tissue. After multiple scattering events, the polarization of incident light cannot be preserved and becomes depolarized. Only single scattered light maintains a high degree of polarization and this preserves the useful characteristic oscillatory structures in the near-back scattered spectra. If the scattered light is collected using a large numerical aperture LSS system which averages over a large range of scattering angles, this usually results in a loss of the useful characteristic oscillatory patterns [18]. Hence, the majority of LSS systems are based on fiber optic probes or use multiple collection apertures [4,9,10,19]. The detection area is limited by the fiber size or the aperture size and the techniques used generally do not involve imaging, making them unsuitable for large area cell morphology surveillance.

With the development of narrow band imaging and multispectral imaging techniques, it has become feasible to acquire multispectral optical image stacks with a high spatial and spectral resolution and large fields of view (FoV). These methods have potential for more meaningful clinical utilization compared with point probe spectroscopy techniques, as images can help to contextualize the data. However, because imaging based on LSS requires detailed knowledge about the collection geometry and polarization properties of the imaging system, few systems—especially endoscopic ones—have been demonstrated for LSS. Exceptions to this include the first LSS based imaging system developed by Backman *et al.* [20,21] which successfully obtained the percentage of enlarged nuclei and the nuclear solid mass to identify adenomatous polyps and inflammatory polyps without dysplasia. However, it was a non-endoscopic imaging system and compromised spectral resolution by using eleven 4 nm bandwidth filters to select illumination wavelengths in the range from 450 nm to 700 nm. An endoscopic instrument using a probe scanning technique was developed by Perelman *et al*. [18] which achieved high spectral performance but for a restricted number of discrete sampling points and a relatively long acquisition time.

Rigid endoscopes are widely used for surgery, because they have high resolution, a wide FoV, a large range of working distances and low chromatic aberrations. It is the aim of this work to create a polarized multispectral imaging system based around a rigid endoscope to detect micron sized particles using LSS. The first part describes the preliminary feasibility analysis for acquiring polarization resolved LSS with a rigid endoscope system and a tunable light source, which includes the study of the polarization properties and entrance pupil of the endoscope. The experimental setup, Mie scattering modeling, and sample preparation are then examined. The instrument was first validated with different sized mono-disperse polystyrene microspheres, then an image was reconstructed based on LSS to illustrate the differentiation of the different microspheres. Finally a preliminary experiment was conducted to demonstrate its capability to discriminate different types of cells.

2. Methods

2.1. Feasibility analysis for polarization detection through a rigid endoscope

The feasibility to implement LSS with a rigid endoscope depends on the polarization properties and the numerical aperture of the endoscope, since the polarization properties of the scattered light must be detected at the proximal end of the endoscope for a number of different wavelengths and over a narrow range of scattering angles. In previous work the polarization response of rigid endoscopes was investigated [22] in order to test how the endoscope affected the transmitted polarization and therefore whether typical rigid endoscopes could be utilized for polarization imaging (Fig. 1(a)). This involved measuring the Mueller matrix of a Karl Storz and Olympus 10 mm laparoscope, and it was found that significant birefringence was

#170838 - $15.00 USD Received 18 Jun 2012; revised 7 Aug 2012; accepted 8 Aug 2012; published 13 Aug 2012

caused by the sapphire window of endoscope. To reconstruct the tissue polarization at the distal end of the endoscope, a Mueller matrix would be required for every pixel in the imaging FoV of the endoscope at every imaging wavelength. These matrices are prohibitively difficult to acquire due to the different geometries required during imaging, as well as the complex wavelength and angular response of commercial wave plates.

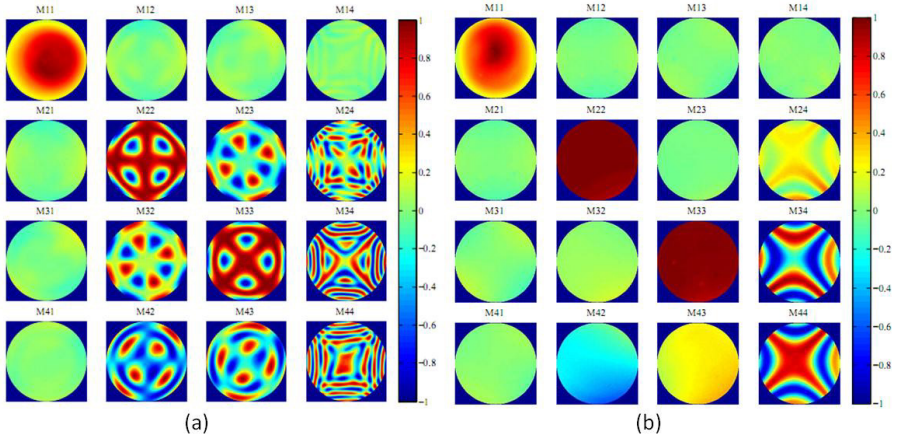

Fig. 1. Measured Mueller matrices for the Storz laparoscope (a) with normal crystal window; (b) with fused silica window. Each sub-image shows one element of the matrix across the whole field.

An alternative solution is to simply replace the sapphire window with fused silica. As preparatory work for the study described in this paper, such an endoscope was provided by Karl Storz GmbH, and the Mueller matrix was measured again using the setup described in Wood *et al*. [22,23]. As shown in Fig. 1(b), the M12, M13, M21, M23, M31, M32, M41, M44 images in the Mueller Matrix remained at zero across the FoV, and therefore the modified laparoscope is equivalent to a non-polarized optical component like an attenuator, making it suitable for polarization resolved endoscopy experiments. The non-zero matrix elements M24, M34, M42, and M43 contained features that could be attributed to the Mueller matrix measurement system used in the experiment.

LSS measurements require the multispectral polarization signal to be recorded over only a narrow range of collection angles. Luckily, conventional endoscopic objective lens systems usually have a small entrance pupil diameter which minimizes third order aberrations over the large field [24]. The entrance pupil of the birefringence-free endoscope was measured to be 0.6 ± 0.05 mm and it was located approximately 2 cm inside the distal end [25]. Therefore when the endoscope was used at a normal working distance (typically several centimeters) the numerical aperture was sufficiently small to preserve information on the characteristic oscillatory spectral patterns and allow observation of changes in this signal with particle size.

2.2. System setup

Figure 2 shows the experimental setup for the polarized multispectral endoscope system. The wavelength tunable illumination system consisted of a supercontinuum laser (SC450-2, Fianium Ltd. UK) and an acousto-optic tunable filter (AOTF, AOTF-VIS Fianium Ltd. UK). The emergent light from AOTF was collimated, linearly polarized with polarization orientation parallel to horizontal plane and could be automatically tuned across the visible range from 400 to 700 nm with a 4-10 nm bandwidth. The beam was expanded and delivered to the sample at an angle of 10 degrees to the sample normal, where it illuminated a circular area with a diameter of 6 mm. An absorber was placed behind the sample to prevent background reflections for optically thin samples. The rigid endoscope was positioned orthogonally to the sample plane at a distance of 2cm and the sample plane was imaged onto a

#170838 - $15.00 USD Received 18 Jun 2012; revised 7 Aug 2012; accepted 8 Aug 2012; published 13 Aug 2012

CCD (Retiga-2000R, Qimaging, Inc., Canada) using an objective lens (SM1NR05, Thorlabs, Inc., US). Thus the distance between the entrance pupil and sample plane is estimated as 4cm. An analyzer was placed in the imaging path and consisted of a linear polarizer (25mm PL, Tamron, Japan) which was aligned to detect either the scattered light polarization parallel or perpendicular to the incident laser light. The CCD and AOTF were controlled by LabVIEW software.

One image every 2 nm from 450 to 700 nm was grabbed. Two image stacks with the analyzer parallel and perpendicular to the illumination polarization were acquired for each sample. The pixel values were extracted from each stack using Matlab, represented by $I_{\parallel}(\lambda)$ and $I_{\perp}(\lambda)$ respectively. In this work, only non-absorbing samples were employed. For non-absorbing samples, the summation of $I_{\parallel}(\lambda)$ and $I_{\perp}(\lambda)$ could be a good approximation of the light source spectrum, hence the linear degree of polarization $DoP(\lambda)$ could be regarded as a good representation of the single scattering spectrum. The scattering spectra in the following results therefore refers to $DoP(\lambda)$ with arbitrary units:

$$DoP(\lambda) = \frac{I_{\parallel}(\lambda) - I_{\perp}(\lambda)}{I_{\parallel}(\lambda) + I_{\perp}(\lambda)}. \quad (1)$$

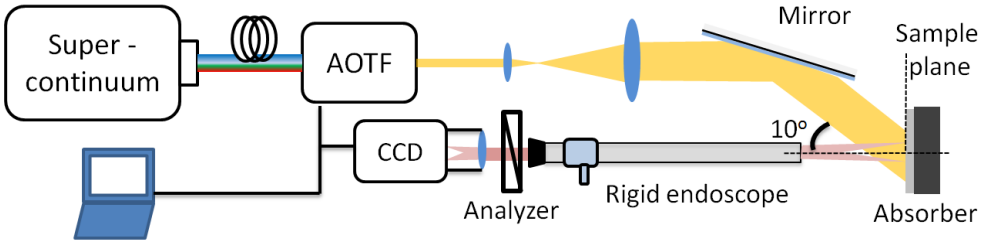

Fig. 2. Experimental setup.

2.3. Modeling the endoscopic multispectral signal

LSS incorporating polarization gating can statistically differentiate multiply scattered photons from the single scattered ones which provide information about the scatterer sizes. There are two approaches to achieving this: the first collects angle-resolved scattered light over a large range of angles for one wavelength; the second collects spectrally-resolved scattered light over a range of wavelengths for one scattering angle. The scattering process can be modeled using a Mie scattering theory as described in the following paragraphs [4].

To model the scattered light that is collected by our modified laparoscope system the approach described by Backman *et al*. [4] is used. A plane electromagnetic wave (linear polarized light) is considered as $\boldsymbol{E_i} = E_i$*exp (ikr-ωt), where E_i is the wave amplitude, k is the wave vector, ω is the frequency, r is the distance and t is the time. The scattered wave is represented by $\boldsymbol{E_s}$ and the scattering plane is that which contains $\boldsymbol{E_i}$ and $\boldsymbol{E_s}$. The distance r for the scattered light is the distance from the particle to the entrance pupil of the imaging system. Furthermore, θ and φ can be defined as the scattering angle and the angle between the polarization direction and the scattering plane respectively and θ is indicated in Fig. 3(a). The incident wave amplitude E_i can be decomposed into two orthogonal components E_{i1} and E_{i2} that are parallel and perpendicular to the plane of scattering, respectively

$$\begin{bmatrix} E_{i2} \\ E_{i1} \end{bmatrix} = \begin{bmatrix} \cos\varphi \\ \sin\varphi \end{bmatrix} E_i. \quad (2)$$

The scattered wave components E_{s1} and E_{s2} which are parallel and perpendicular to scattering plane can be derived by means of scattering amplitude matrix of homogeneous spherical particles [26] using the following relationship:

#170838 - $15.00 USD Received 18 Jun 2012; revised 7 Aug 2012; accepted 8 Aug 2012; published 13 Aug 2012

$$\begin{bmatrix} E_{S2} \\ E_{S1} \end{bmatrix} = \begin{bmatrix} S_2(\theta) & 0 \\ 0 & S_1(\theta) \end{bmatrix} \begin{bmatrix} E_{i2} \\ E_{i1} \end{bmatrix}. \tag{3}$$

S_1 and S_2 denote Mie scattering amplitudes. The amplitudes E_{s1} and E_{s2} are related to $E_{s\parallel}$ and $E_{s\perp}$ which are the projections of scattering field onto the direction and the orthogonal direction of E_i, respectively:

$$\begin{bmatrix} E_{S\parallel} \\ E_{S\perp} \end{bmatrix} = \begin{bmatrix} \cos\varphi & \sin\varphi \\ \sin\varphi & -\cos\varphi \end{bmatrix} \begin{bmatrix} E_{S2} \\ E_{S1} \end{bmatrix}. \tag{4}$$

Substituting Eq. (2) and Eq. (3) into Eq. (4),

$$\begin{aligned} \begin{bmatrix} E_{S\parallel} \\ E_{S\perp} \end{bmatrix} &= \begin{bmatrix} \cos\varphi & \sin\varphi \\ \sin\varphi & -\cos\varphi \end{bmatrix} \begin{bmatrix} S_2(\theta) & 0 \\ 0 & S_1(\theta) \end{bmatrix} \begin{bmatrix} \cos\varphi \\ \sin\varphi \end{bmatrix} E_i \\ &= \begin{bmatrix} -S_2(\theta)\cos^2\varphi + S_1(\theta)\sin^2\varphi \\ -S_2(\theta)\sin\varphi\cos\varphi - S_1(\theta)\sin\varphi\cos\varphi \end{bmatrix} E_i. \end{aligned} \tag{5}$$

According to Eq. (5), the scattered intensities $I_{\parallel}(\lambda)$ and $I_{\perp}(\lambda)$ and are related to the intensity of incident light I_0:

$$I_{\parallel} = \frac{I_0}{k^2 r^2}\left(|S_2|^2 \cos^4\varphi + |S_1|^2 \sin^4\varphi - 2\,\mathrm{Re}(S_1 S_2^*)\sin^2\varphi\cos^2\varphi\right), \tag{6}$$

$$I_{\perp} = \frac{I_0}{k^2 r^2}\left(|S_2|^2 + |S_1|^2 + 2\,\mathrm{Re}(S_1 S_2^*)\right)\sin^2\varphi\cos^2\varphi. \tag{7}$$

Hence, the differential intensity ΔI between the intensity in the two polarization states can be expressed as

$$\Delta I = \frac{I_0}{k^2 r^2}\left\{\left(|S_2|^2 \sin^2\varphi - |S_1|^2 \cos^2\varphi\right)\left(\sin^2\varphi - \cos^2\varphi\right) - 4\,\mathrm{Re}(S_1 S_2^*)\sin^2\varphi\cos^2\varphi\right\} \tag{8}$$

and is a function of wavelength λ, scattering angle θ, polarization orientation φ, and refractive index n. $\Delta I(\lambda)$ is an expression for the wavelength dependent elastic scattering spectrum that is to be measured.

The differential signal $\Delta I(\lambda)$ detected with the polarized multispectral endoscopic imaging system depends on the size of the entrance pupil of the imaging system as well as the bandpass filtering function of the tunable filter. A range of scattered light rays passing through the entrance pupil at different scattering angles θ and polarization orientation φ angles contribute to the final signal as indicated Fig. 3(a). This range can be represented by a solid angle Ω, which is equivalent to the concept of numerical aperture and is defined by the entrance pupil and working distance. Since the Mie scattered light has an angular distribution (an example is given by the blue polar plot in Fig. 3(b)), the detected signals suffer from a reduction in modulation caused by the integration over the collection solid angle Ω. Fortunately as shown in section 2.1 this is relatively small for standard laparoscopes. The spectral bandwidth of the tunable filter also creates a signal modulation smoothing effect due to the small but finite bandwidth of the filtered light. Assuming that the filtering function of the tunable filter is fixed at each working wavelength, the effect can be described by a convolution with the filter response. Hence, the final signal can be expressed as follows:

$$\Delta I(\lambda) = T(\lambda) * \iint_{\Omega} \Delta I(\lambda, \theta, \varphi) d\Omega \tag{9}$$

#170838 - $15.00 USD Received 18 Jun 2012; revised 7 Aug 2012; accepted 8 Aug 2012; published 13 Aug 2012

where the ranges of integration of θ, φ are confined by Ω, and $T(\lambda)$ denotes the bandpass filtering function of the tunable filter. Considering the size distribution of scatterers follows $F(dia)$, Eq. (9) can be further rewritten as

$$\Delta I(\lambda) = T(\lambda) * \iint_{\Omega} \left[\int \Delta I(\lambda, dia, \theta, \varphi) \times F(dia) d(dia) \right] d\Omega. \quad (10)$$

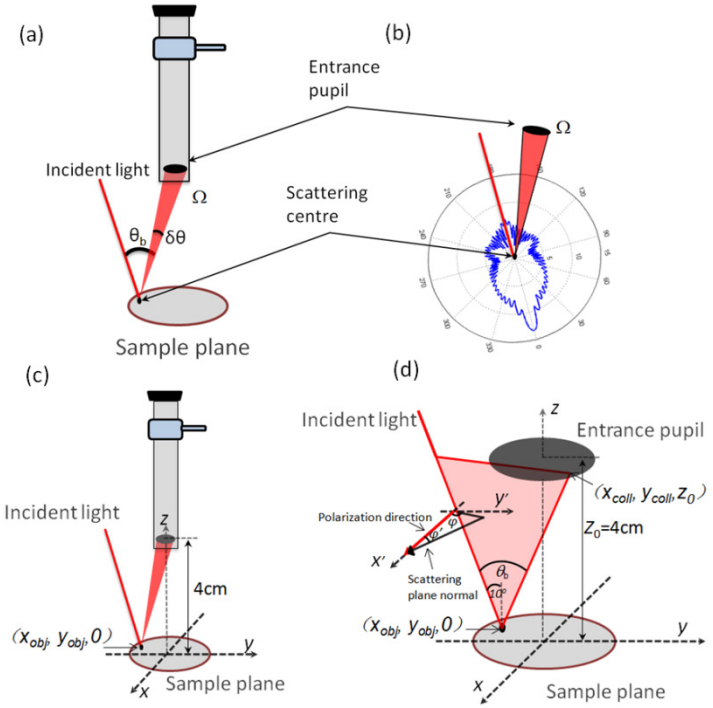

Fig. 3. (a) sketch of collection geometry of a rigid endoscope. A collection solid angle Ω is defined by the entrance pupil and working distance. The scattered light rays within this solid angle are collected. θ_b in this figure is the supplementary angle of θ; (b) the blue polar plot is the angular scattering intensity distribution of 5 μm polystyrene microsphere at 532 nm. If several peaks and troughs are collected by the endoscope, the eventual signal suffers from a reduction in modulation caused by the integration over the collection solid angle; (c) lab reference coordinate system used for modeling the scattering process. (d) Sketch of the substitution of a lab reference coordinate system for θ and φ. x_{obj}, y_{obj}, x_{coll} and y_{coll} were substituted for θ and φ based on analytic geometry. The plane of scattering is plotted as the red triangle. (x_{obj}, y_{obj}, 0) refers to the position of a scatterer on the sample plane within the system FoV, and (x_{coll}, y_{coll}, z_0) indicates the position of a point inside the entrance pupil S. φ_0 is 90°, and thus the polarization direction is parallel to x. The angle between the plane of scattering and the y-z plane φ' can be derived first. φ is the angle between the polarization direction and the scattering plane. φ is derived according to the relationship $\varphi = \varphi_0 - \varphi'$. In the figure, with φ_0 = 90°, φ and φ' are complementary angles.

Transforming Eq. (10) into the lab reference coordinate system where the x and y axes are a pair of orthogonal vectors in the object plane yields

$$\Delta I(\lambda, x_{obj}, y_{obj}) = T(\lambda) * \iint_{S} \left[\int \Delta I(\lambda, dia, x_{coll}, y_{coll}, x_{obj}, y_{obj}) \times F(dia) d(dia) \right] dS, \quad (11)$$

where (x_{obj}, y_{obj}, 0) refers to the position of the scatterers on the sample plane within the system FoV as shown in Fig. 3(c), and (x_{coll}, y_{coll}, z_0) indicates the position of a point inside the entrance pupil. z_0 is the distance between entrance pupil and the x-y plane (sample plane) and corresponds to the working distance of endoscope. x_{obj}, y_{obj}, x_{coll} and y_{coll} were substituted for θ

#170838 - $15.00 USD Received 18 Jun 2012; revised 7 Aug 2012; accepted 8 Aug 2012; published 13 Aug 2012

and φ based on analytic geometry. In the lab reference coordinate system, the equation of the incident ray is determined by (x_{obj}, y_{obj}, 0) and its propagation orientation which is 10° to the normal of sample plane and is parallel to the y-z plane (Fig. 3(d)). The equation of the scattered ray can also be derived from (x_{obj}, y_{obj}, 0) and (x_{coll}, y_{coll}, z_0). Then θ, which is the angle between the two rays, as well as the equation of the plane of scattering, can be obtained. The angle between the plane of scattering and the y-z plane, φ', can be derived first. The angle between the polarization orientation of the incident light and the y-z plane is φ_0 (which is set to be 90° in the experiment). Thus φ equal to $\varphi_0 - \varphi'$ can be expressed by x_{obj}, y_{obj}, x_{coll}, and y_{coll}. The bounds of the integration S correspond to the limits of Ω, and can be expressed as $x_{coll}^2 + y_{coll}^2 < r_0^2$, where r_0 denotes the radius of the endoscope entrance pupil. $\Delta I(\lambda, x_{obj}, y_{obj})$ corresponds to the signal at a pixel directly on the image plane.

2.4. Sample preparation

Mono-disperse polystyrene microspheres are widely used low absorption scattering particles. The system validation experiments used diameters ranging from 0.5 μm to 10 μm (refractive index n = 1.59, Polyscience, Inc., Warrington, PA) diluted by distilled water (refractive index n = 1.33). The aqueous microsphere samples were held in a 24 well plate (BD Falcon) and the microspheres were homogeneously distributed before use through by stirring with a spatula. In the image reconstruction experiment, two pipettes with sealed distal ends were used to hold 0.5 μm and 1 μm microsphere samples respectively.

For the cell sample experiments two types of cell line, OSEC2 (healthy ovarian cells) and A549 (lung cancer cells), were employed to construct a two layer phantom. The substrate layer consisted of 2% agar and 0.5% Intralipid to simulate the diffusive background scattered light in tissue. The surface was covered with cell suspensions in 20% Bovine Serum Albumin (BSA) to reduce the mismatch in refractive index between cytoplasm and surrounding environment and minimize the unrealistic influence of scattering signals from the whole cell body.

3. Results and Discussion

3.1. System validation with known size mono-disperse polystyrene microspheres

In this validation experiment, the average value for a 10 by 10 pixel area in the center of the FoV was extracted from each stack using Matlab, represented by $I_{\parallel}(\lambda)$ and $I_{\perp}(\lambda)$ respectively. The $DoP(\lambda)$ was further calculated to represent the single scattered spectrum. Figure 4 demonstrates the scattering spectra of different sized polystyrene microspheres. The spectral patterns of each size microsphere sample are unique. The simulated spectrum for the 1 μm beads based on the model discussed in section 2.3 shows a high similarity to the experimental data. By comparing the spectra of Fig. 4 (a) and (c-f), the modulation frequency of the oscillatory spectral patterns also exhibits a strong correlation dependence on microsphere size, as predicted by Mie scattering theory. The oscillatory spectral pattern of the 6 μm microspheres in Fig. 4(e) is not as conspicuous as those of the 0.5 μm, 1 μm and 2 μm ones. The spectrum exhibits poor contrast of the periodic peaks and troughs in the oscillatory pattern. This can be attributed to the convolution effect caused by the 6-10 nm bandwidth of the AOTF and the small entrance pupil of this endoscopic system. The oscillatory pattern from 670 to 700 nm can be better distinguished because the oscillatory frequency decreases gradually as the wavelength increases. Although the high frequency details in the oscillatory patterns of the 6 μm and 10 μm microspheres cannot be observed very clearly, the unique profiles of the spectral patterns still preserve information about their sizes. This validation experiment confirms that our polarized multispectral endoscopic system can acquire elastic scattering spectra that contain abundant information of scatterer size and that the acquired spectrum can be matched to the model.

#170838 - $15.00 USD Received 18 Jun 2012; revised 7 Aug 2012; accepted 8 Aug 2012; published 13 Aug 2012

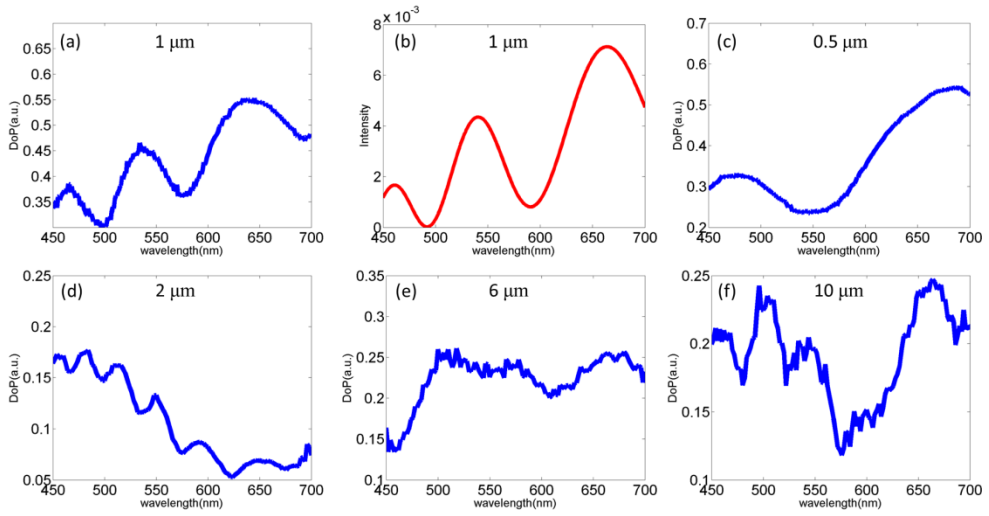

Fig. 4. Scattering spectra of different sized polystyrene microsphere samples. (a) Experimental and (b) simulated spectrum of 1 μm diameter microspheres in water; (c-f) Experimental scattering spectrum of 0.5μm, 2μm, 6μm and 10 μm microspheres in water.

3.2. Image reconstruction

The 0.5 μm and 1 μm microsphere solutions were held in two neighboring isolated pipettes and images were recorded with the endoscope system using a 6 x 3 mm FoV and 2 cm working distance. Some of the raw images from the multispectral stack are displayed in Fig. 5(a), showing the 0.5 μm well at the top and the 1 μm well at the bottom, although the two scatterer types could not be distinguished. After extracting the scattering spectra, a clear difference between the wells could be observed as shown in Fig. 5(b). These spectra were taken from two 10 by 10 pixels regions indicated by two squares in Fig. 5(a). To illustrate how this data can be represented as an image, a ratio was calculated for each pixel by dividing the mean *DoP* value in 655-665 nm region by the mean *DoP* value in 535-545 nm region, as indicated by the blue rectangles in Fig. 5(b). The resulting greyscale images are shown in

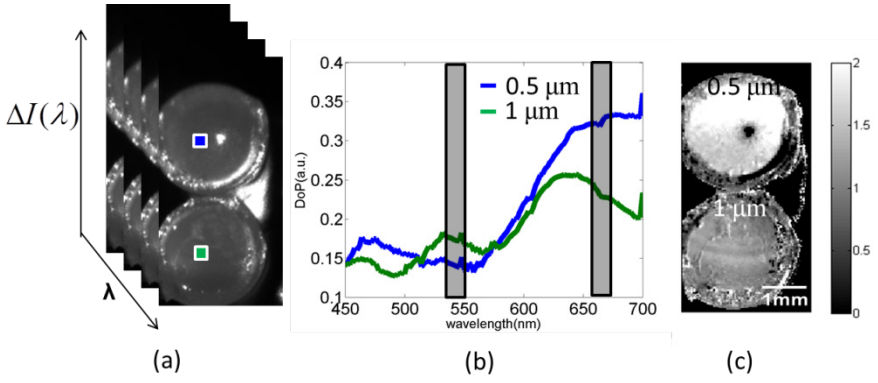

Fig. 5. (a) Representative polarization and spectrally resolved images from the stack of raw images used to extract the scattering spectra. The upper sample contains 0.5 μm microspheres and the lower one contains 1 μm microspheres. The region marked by blue and green squares was used to generate scattering spectra in (b); (b) The scattering spectra of the 0.5 μm (blue) and 1 μm microspheres (green), with the spectral regions around 660 nm and 540 nm used to construct the ratiometric images indicated by the blue rectangles; (c) The ratiometric image after intensity merging. The ratios for the 0.5 μm and 1 μm microspheres are around 2 and 1.25 respectively.

#170838 - $15.00 USD Received 18 Jun 2012; revised 7 Aug 2012; accepted 8 Aug 2012; published 13 Aug 2012

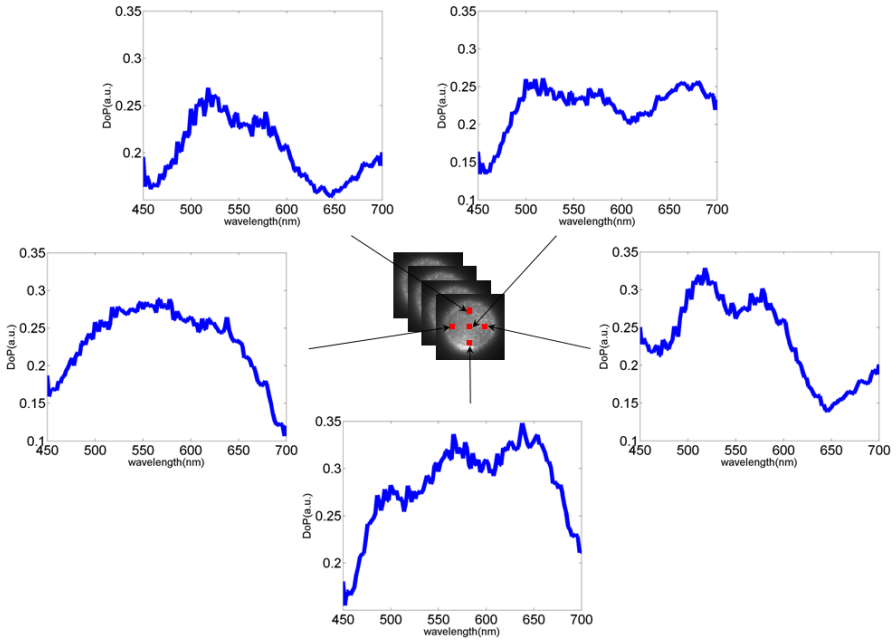

Fig. 6. Variation in scattering spectra of 6 µm microspheres extracted at five different 10 by 10 pixel regions as indicated by the five red squares in the central image.

Fig. 5(c) where the background signal has been intensity thresholded out. The ratios for the 0.5 µm and 1 µm microspheres are around 2 and 1.25 respectively. The two different sized microsphere samples are easily distinguished in the image illustrating the robustness of the *DoP* spectra across the FoV.

When reconstructing images for the 6 µm and 10 µm microspheres, the spectral patterns across the field of view were found to vary significantly. For instance Fig. 6 displays the scattering spectra for the 6 µm microspheres extracted from five different 10 by 10 pixel regions within the FoV. The scattering spectra are not identical and the most probably reason for this is that the scattering angle at each position is not exactly the same, leading to a nonuniform spectral pattern even in this relatively small FoV (5 x 5 mm). The range of different scattering angles within the FoV can be calculated based on geometry and parameters used in the current setup as indicated in Fig. 7(a). The scattering angle was calculated for each pixel within the FoV and it was found that there was a variation of 7° from one side to the other, as indicated in Fig. 7(c). To further confirm the assumption that this could cause the observed variations in scattering spectrum, the modeling code was used to simulate the scattering spectrum for an angle of 170° (center of FoV), as well as at 165 °, 166°, and 175°. This process was also repeated for the 1 µm and 6 µm microspheres and the results are displayed in Fig. 8. Few differences are observed in the scattering spectra for the 1 µm microspheres, but in contrast, the spectral patterns of the 6 µm microspheres changed significantly. Even for a scattering angle increase of 1°, there is little similarity between the spectra, consistent with the experiment.

Whilst the variation in scattering angle across the FoV could be taken into account, one possible solution is to employ an illumination delivery fiber rather than using a collimated light source, and in addition this would also allow the fibers within the endoscope itself to be used for light delivery. To test the hypothesis that the variation in scattering angle would be reduced in this case another simulation was run using the geometry indicated in Fig. 7(b). In the simulation, the distal end of an optical fiber had a numerical aperture of 0.12 and the fiber tip and entrance pupil of the laparoscope were both 2 cm away from object plane. The fiber

#170838 - $15.00 USD Received 18 Jun 2012; revised 7 Aug 2012; accepted 8 Aug 2012; published 13 Aug 2012

was angled at 10° to the orientation of the endoscope, which was normal to the object plane as indicated in Fig. 7(b). The results of the simulation are shown in Fig. 7(d) showing a very even scattering angle distribution. The variation across this 5 x 5 mm FoV is smaller than 0.5°, while for parallel illumination it reached 7°. Since the light emerging from AOTF is linearly polarized a polarization maintaining fiber could be employed to deliver the light and to guarantee illumination efficiency.

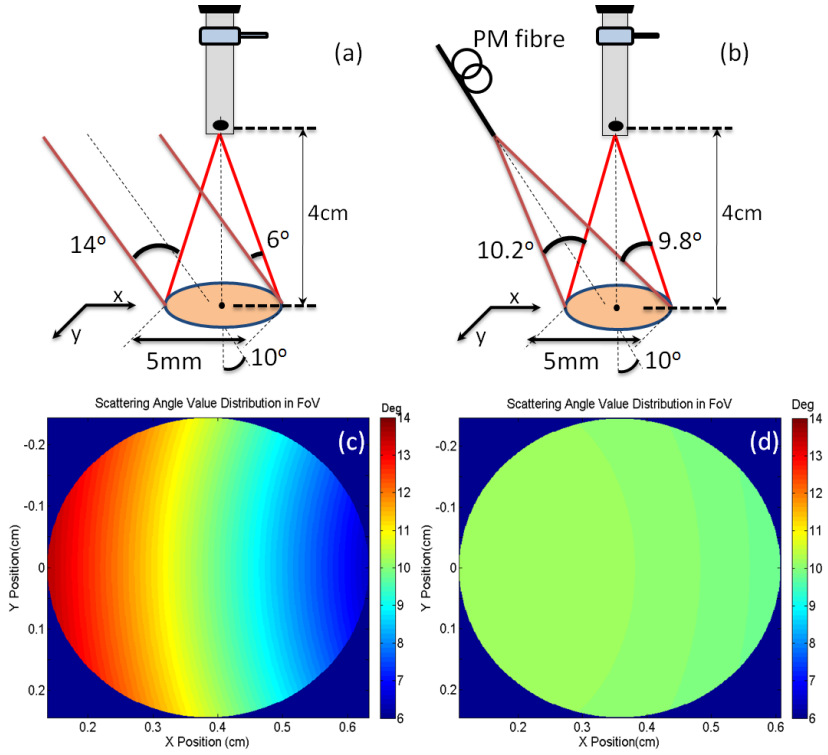

Fig. 7. (a), (b) Schematic for parallel illumination and fiber illumination respectively; (c), (d) Scattering angle distribution for parallel illumination and fiber illumination respectively.

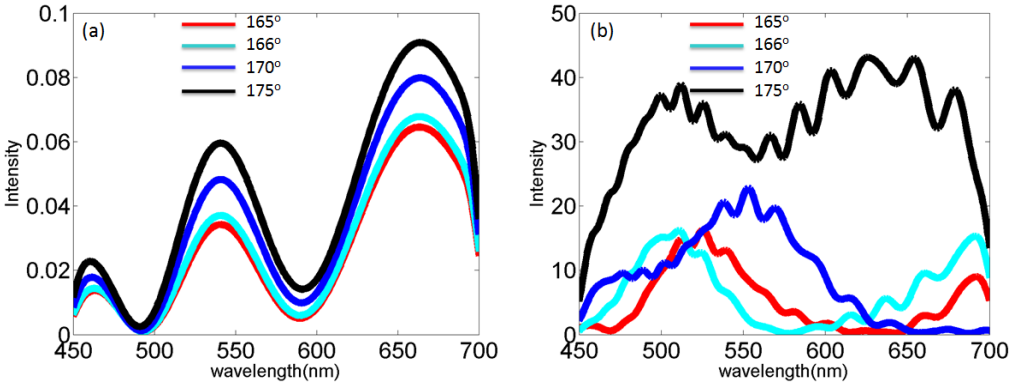

Fig. 8. Simulated scattering spectra of 1 µm (a), 6 µm (b) at different scattering angles: 165° (red), 166° (cyan), 170° (blue) and 175° (black) respectively.

#170838 - $15.00 USD Received 18 Jun 2012; revised 7 Aug 2012; accepted 8 Aug 2012; published 13 Aug 2012

3.3. Preliminary cell experiment

Photos of cell suspension recorded with a phase contrast microscope in Fig. 9 confirm that 20% BSA reduces the refractive index mismatch between cytoplasm and surrounding medium in order to minimize the impact of cytoplasm scattering, which has been reported to have a small contribution compared to nuclei in tissue scattering [19].

Measurements were conducted on three batches of A549 and OSEC2 cells. Only average pixel values within a 10 x10 pixel area in the center of the FoV were extracted. The scattering spectra were obtained as shown in Fig. 10. The spectra marked by green in Fig. 10(a) and marked by green and blue in Fig. 10(b) have a larger average of *DoP* values. This is caused by the variation of optical thickness $OT = u_s z$ with u_s the scattering coefficient and z thickness of cell suspensions. *OT* is related to the concentration and the thickness of cell suspensions. Less multiple scattering events in the suspension with a smaller *OT* mean the suspension has less possibility to depolarize the incident light and thus demonstrates a larger average *DoP* value. *OT* does not have a significant influence on the spectral pattern. This may be the reason why the spectral profiles of OSEC2 cells maintain a similar pattern with a peak at 600 nm and a trough at 650 nm. By contrast, the spectral patterns of A549 cells have a smooth increasing trend. The difference between the two types of cells can be consistently observed which may

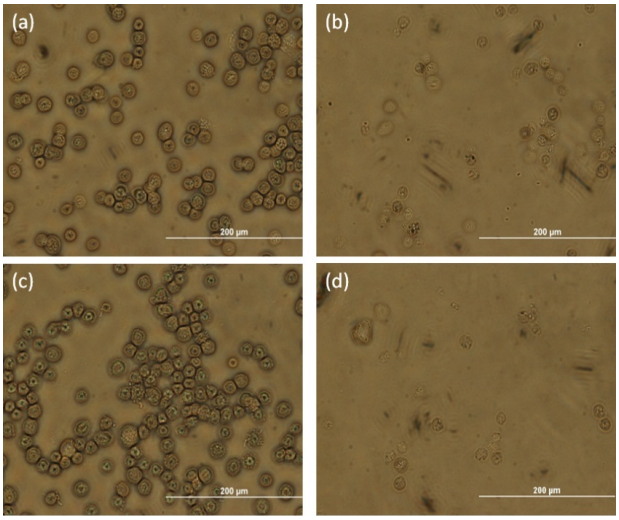

Fig. 9. Photos of cell suspension recorded with a phase contrast microscope. (a) OSEC2 cell suspension; (b) OSEC2 cells in 20% BSA; (c) A549 cells; (d) A549 cells in 20% BSA. The concentration of cells in (a-d) is the same.

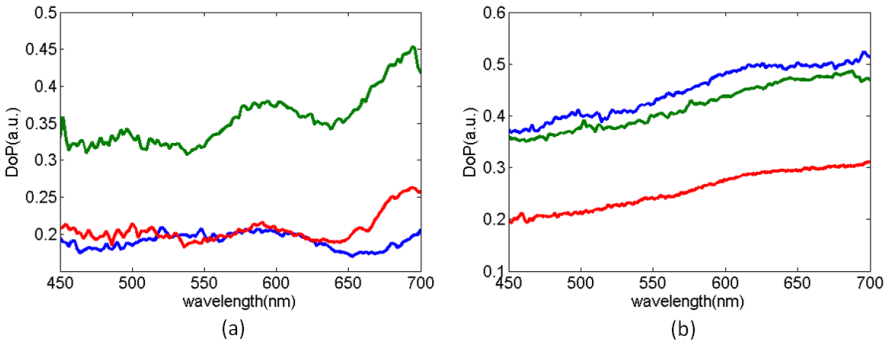

Fig. 10. Scattering spectra of three batches of (a) OSEC2 and (b) A549cells in 20% BSA solution

#170838 - $15.00 USD Received 18 Jun 2012; revised 7 Aug 2012; accepted 8 Aug 2012; published 13 Aug 2012

be from the scattering of different sized nuclei, and these are similar to previous results reported in [4]. The scattering patterns over the field are not uniform, which may indicate that the light scattering is more similar to the larger microsphere samples in section 3.2. Because the cell suspensions were not very concentrated, part of single scattering signals may also come from Intralipid substrate, although the results indicate that the weak cell scattering signal can still be detected.

4. Conclusion

Our work has shown for the first time that polarized multispectral imaging in a rigid endoscope based on LSS is feasible. Polystyrene microspheres of different sizes were successfully discriminated based on their polarized LSS spectra, and images could be created from these spectra. A preliminary experiment on different cell types also demonstrates that the system can differentiate between these, probably due to the different size distributions of the scatterers. A fiber illumination system was proposed for reducing the FoV-dependent change in scattering signal, and future work will focus on improving the system by incorporating this approach as well as further imaging living cells and tissue.

Acknowledgments

Funding for this project was provided by ERC grant 242991. Ji Qi acknowledges support from the China Scholarship Council. We would like to thank Karl Storz GmbH for assistance with the rigid endoscope.

#170838 - $15.00 USD Received 18 Jun 2012; revised 7 Aug 2012; accepted 8 Aug 2012; published 13 Aug 2012